

Controllable Cetrinide – Assisted Hydrothermal Synthesis of MoFe_2O_4 and Coupling with Al_2O_3 as an Effective Photocatalyst for Decolorization of Indigo Carmine Dye

Mohammed Ali Hameed and Luma Majeed Ahmed*

Department of Chemistry, College of Science, University of Kerbala, Kerbala 56001, Iraq

* **Corresponding author:**

tel: +964-7801683055

email: luma.ahmed@uokerbala.edu.iq

Received: July 8, 2023

Accepted: August 4, 2023

DOI: 10.22146/ijc.86693

Abstract: This research focuses on the MoFe_2O_4 nanoparticles synthesized via the hydrothermal method in the presence of positive surfactant- Cetrinide (CT) as a template and stabilizer. This is vital to prevent the agglomeration and reducing its activity. The mean crystal sizes of MoFe_2O_4 and its composite with alumina system were observed to be 23.97 and 47.41 nm, respectively. The shapes of MoFe_2O_4 and its composite are nanoplate and like-popcorn nanoparticles. The EDX spectra demonstrated that the MoFe_2O_4 and its composite are truly synthesized with high purity. The FTIR proved the MoFe_2O_4 is normal spinel. Based on the Tauc equation, band gaps were measured and found to be 2.78 and 4.05 eV for MoFe_2O_4 and its nanocomposite. The photo decolorization efficiency (PDE) of indigo carmine dye (IC) using MoFe_2O_4 nanoparticles and its nanocomposite was discovered to be 90.84 and 91.50%, respectively, at pH 5.3, 10 °C for 50 min. This photoreaction obeys the pseudo-first order, exothermic, spontaneous, and negative activation energy, that attitude to the multi-step occurs in chain reactions. This behavior depends on the speed of the binding step of the dye with Fe^{3+} , Mo^{6+} , or Al^{3+} in the crystal lattice of MoFe_2O_4 nanoparticle and its nanocomposite.

Keywords: hydrothermal method; positive surfactant; molybdenum ferrite nanoparticle; spinel; indigo carmine dye

■ INTRODUCTION

In recent years, interest in effluent treatment technology has become widespread due to the organic pollutants in water that constitute a serious threat to the ecological environment of humans and other living things. Most methods are applied to remove or degrade such as adsorption [1-3], Fenton, photo-Fenton [4-5], photolysis, and photocatalysis [6-7]. One of the potential effluent treatment methods is the photocatalytic process, which can decompose or decolorize hazardous organic contaminants in an environmentally acceptable manner [8-10].

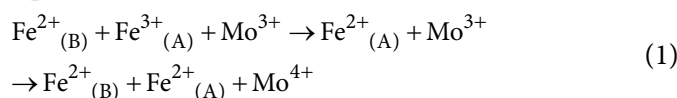
Hence, many scientists are devoted to developing new photocatalysts with high efficiency to address the challenges of water pollution [11-14]. Since visible light radiation accounts for 50% of all solar energy absorbed by the planet, semiconductor photocatalysts, particularly those powered by visible light, have drawn significant interest [15]. Thus, designing and implementing high-efficiency,

low-cost, and stable photocatalysts driven by visible light is highly desirable for practical applications that attitude to the high toxicity and hazard of dyes. Hence, there are a variety of paths to eliminate them from wastewater via adsorption, oxidation, photocatalysis, membrane filtration, photodegradation, and irradiation [16-17].

Spinel nanocrystals are two of the most important inorganic nanomaterials with distinct magnetic, electronic, optical, catalytic, and electrical properties. The structure of spinel makes up the AB_2O_4 , A and B are represented by the tetrahedral and the octahedral binary cation and trinity cation binding sites, respectively. The O indicates the position of the oxygen anion. The spinel ferrite metal is a widespread and vital exam for spinel materials. The general molecular formula is MFe_2O_4 (M = Mo, Mn, Zn, Co, Ni, or Mg), which has a face-centered-cubic (fcc) tight packing structure. A great deal of research has been done on the metal ferrites in this area as inverse, normal, and mixed-use buildings are all

unique architectural shapes. The spinel crystal forms exhibit excellent chemical stability, low coercivity, strong electromagnetic conductivity, low-loss materials, mechanical hardness, good performance, high-frequency soft magnets, and moderate saturation magnetization [18-19].

The MoFe_2O_4 is viewed as one of the inverse spinel materials with a cubic spinel oxide, which has peculiar magnetic properties and has been studied by numerous researchers [20]. The inverse spinel MoFe_2O_4 includes that the cations present in the octahedral and tetrahedral sites of the spinel lattice are Fe^{2+} , Fe^{3+} , Mo^{3+} and Mo^{4+} and the formal valence assignment can be best represented by Eq. (1):



Domenichini et al. [21], confirmed the presence of Mo^{3+} in MoFe_2O_4 depending on infrared spectrometry, electrical conductivity, derivative thermogravimetry and X-ray photoelectron spectroscopy analysis.

Alumina is one of the greatest matrices for introducing popular oxide supports for metal catalysts as well as metallic nanoparticles. Alumina films and coatings offer exceptional thermal, chemical, corrosion, and radiation resistance. They are also highly transparent, have a huge surface area, and have a narrow band gap. As a result, alumina films are frequently utilized in membrane technology, optoelectronics, aerospace, microelectronic devices as gate insulators, sensors as an antireflective coating, and catalysis [22]. This work seeks to easily create MoFe_2O_4 using the hydrothermal technique in the presence of the positive surfactant (Cetramide) as a template, then fabricate its surface with Al_2O_3 as a nanocomposite via indirect ultrasonic waves. With various analytical tools, the structural, morphological, and optical properties were examined. Additionally, comparative analyses of the decolorization abilities of indigo carmine dye (IC) in individual studies using MoFe_2O_4 and their composite with Al_2O_3 have been carried out. To determine the perfect appropriate conditions for the decolorization of indigo carmine dye, the effects of the initial pH in the solution and the temperature were estimated.

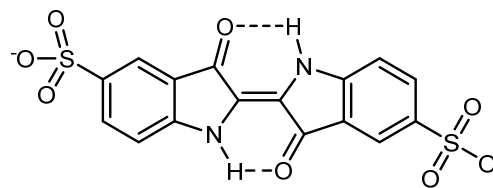


Fig 1. The structure of IC dye

■ EXPERIMENTAL SECTION

Materials

The materials used in this study were the ferric nitrate ($\text{Fe}(\text{NO}_3)_3 \cdot 9\text{H}_2\text{O}$) and sodium molybdate ($\text{Na}_2\text{MoO}_4 \cdot 2\text{H}_2\text{O}$) as powders purchased by Sigma Chemical Corp., USA. Hydrochloric acid (35%) was supplied from the general drug house. Absolute ethanol ($\text{C}_2\text{H}_5\text{OH}$) and CT as a template were purchased by Sigma-Aldrich Chemie. The IC dye ($\text{C}_{16}\text{H}_8\text{N}_2\text{Na}_2\text{O}_8\text{S}_2$) was also purchased by Sigma-Aldrich Chemie. This dye is acidic type, molar mass = 466.36 g/mol, $\lambda_{\text{max}} = 600$ nm and the structure is shown in Fig. 1 [23].

Instrumentation

The instrumentations used in this study were Shimadzu's Lab X-XRD 6000 X-ray diffraction spectroscopy, Kyky's EM-320 scanning electron microscopy with energy dispersive X-ray spectroscopy, Shimadzu's 8400S FTIR spectrometers, and Shimadzu's 1800 UV-visible spectrophotometer were used to characterize the prepared samples. Simple equipment like sensitive balance (Sartorius, BL 210 S), pH meter (OAICTON-2100), ultrasonic (DAIHAN Scientific), magnetic stirrer (Heido-MrHei-Standard), centrifuge (Hettich-Universal II), and furnace (Muffle furnace Size-Tow Gallenkamp) were utilized in preparation and application steps. Several assisted tools for this work were used, such as the hydrothermal technique was used (Steeliness steel with white Teflon tube autoclave type TOPT-HP100 TOPTION), and the ultraviolet lamp (HPML, 400 W, Radium) was used as a crucial component in a homemade photoreactor.

Procedure

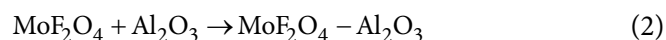
Synthesis of MoFe_2O_4

MoFe_2O_4 nanoplates were synthesized using a hydrothermal method. In a typical synthesis, 35 mL of

distilled water was used to dissolve 2.828 g of $\text{Fe}(\text{NO}_3)_3 \cdot 9\text{H}_2\text{O}$, 25 mL of distilled water and 10 mL of HCl were used to dissolve 0.846 g of $\text{Na}_2\text{MoO}_4 \cdot 2\text{H}_2\text{O}$. At room temperature, the Na_2MoO_4 solution was mixed with the $\text{Fe}(\text{NO}_3)_3$ solution and vigorous stirring. CT powder (0.5 g) was added as a template and a stabilizer with stirring for 15 min to the last mixture. The resulting yellow mixture was transported to a 100 mL Teflon-lined autoclave. The autoclave was then sealed and maintained at 180 °C for 5 h. Subsequently, the autoclave was then cooled to ambient temperature for 2 h. Following filtration, the resultant solid brown sample was repeatedly washed with ethanol and distilled water to ensure that any precursor salt-positive ions and humidity were eliminated. In the desiccator, this precipitate was allowed to dry it using silica gel overnight. The MoFe_2O_4 sample was finally obtained after grinding the dry precipitate to a homogenous powder.

Synthesis of $\text{MoFe}_2\text{O}_4/\text{Al}_2\text{O}_3$ nanocomposite

The 1:2 ratio was prepared from 1 g MoFe_2O_4 : 2 g Al_2O_3 nanocomposite as w/w ratio that was dispersed in 60 mL of ethanol using an ultrasonic wave. The MoFe_2O_4 solution and Al_2O_3 solution were dispersed for 2 h at 75 °C using ultrasonic waves at 65 kHz. The MoFe_2O_4 solution was gradually added to the Al_2O_3 solution and went on for 2 h at 75 °C to perform the linked process between MoFe_2O_4 and Al_2O_3 , according to Eq. (2). The produced light brown precipitate was filtered, then washed with water and ethanol, and stored overnight in a desiccator.



Photoreaction of IC dye with photocatalysts

The decolorization of IC dye was carried out utilizing these catalysts. In Fig. 2, a homemade photoreactor was used to apply the photoreaction. This photoreactor includes 400 watts Philips UV-A lamp with a light intensity equal to 2.95×10^{-7} Einstein s^{-1} . The reactor's body is made of a wooden box covered in aluminum foil to focus the light while also blocking out potential hazards. Inside, there is a magnetic stirrer, a 500-mL Pyrex glass beaker, a teflon bar, and a fan to regulate the temperature [16].

At different temperatures (10, 15, 20 and 25 °C) and with initial dye pH 5.3, a 0.1 g of studied photocatalysts was dispersed in 25 ppm of 100 mL IC dye solution. Without irradiation, the produced suspension solution was magnetically stirred for 15 min to allow for an equilibrium adsorption state to be reached [19]. After the adsorption step, this suspension was exposed to UV light, and then about 3 mL aliquots were collected at irradiation intervals of up to 100 min (3 mL were withdrawn every 10 min). The collected suspensions were separated twice by centrifuge for 15 min, and the resultant filters' absorbance was recorded at 600 nm using UV-visible spectroscopy. The rate constant (k_{app}) and photo decolorization efficiency percentage (PDE%) were found depending on the following equations [24-28];

$$\ln\left(\frac{C_o}{C_t}\right) = k_{\text{app}} \times t \quad (3)$$

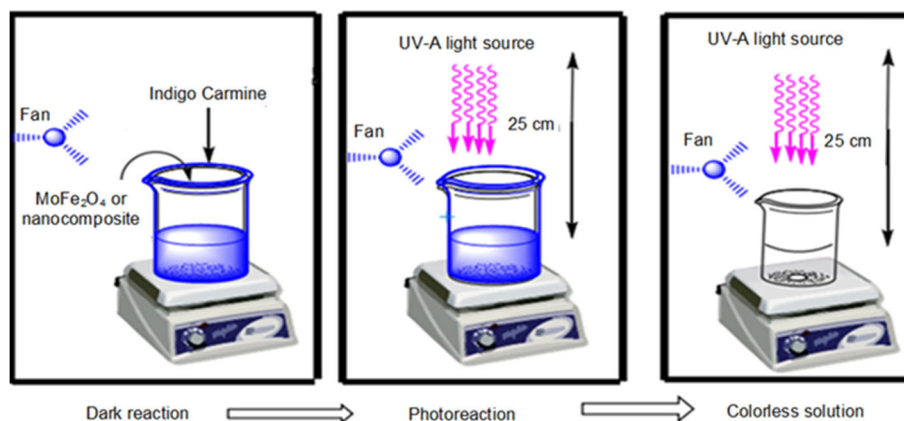


Fig 2. Schematic diagram of homemade photocatalytic reactor unit

$$\text{PDE\%} = \frac{(C_o - C_t)}{C_o} \times 100 \quad (4)$$

where C_o is the initial concentration of dye at the adsorption process, and C_t is residue dye concentration after irradiation.

RESULTS AND DISCUSSION

XRD Analysis

The crystalline peaks were indexed and were found to be in good agreement with the standard monoclinic structure of MoFe_2O_4 [29-30]. Fig. 3. The essential diffraction peaks of monoclinic MoFe_2O_4 appear at $2\theta = 18.36^\circ, 18.91^\circ, 19.60^\circ, 20.56^\circ, 21.20^\circ, 21.86^\circ, 23.01^\circ, 25.79^\circ$ and 27.54° , with miller indicates (200), (220), (-123), (212), (122), (-105), (224), (400) and (503) respectively, the stronger intensity at 2θ for 23.01, 25.79, and 27.54 of the reflection peaks of (224), (400), and (503) which is in good agreement with the literature values (JCPDS 35-0183) [30]. Besides, the Al_2O_3 peaks appear at diffractions (311), (400), (511), (440), (731), and (800) with 2θ positions are $35.17^\circ, 43.37^\circ, 52.56^\circ, 57.51^\circ, 66.53^\circ, 68.22^\circ$ and 76.88° , respectively. These results are agreement with the standard diffraction data (JCPDS card 10-0425) [31].

When the MoFe_2O_4 and Al_2O_3 incorporate as nanocomposite, some essential peaks are shifted toward the high 2θ from 23.01° MoFe_2O_4 and 43.37° Al_2O_3 to 43.52° , from 52.56° Al_2O_3 to 52.71° , from 25.79° MoFe_2O_4 to 27.54° [32]. The very high peak intensity suggests that the material is highly crystalline. This shift in the position of peaks indicates to metallic bond form and incorporates MoFe_2O_4 with Al_2O_3 as $\text{MoFe}_2\text{O}_4/\text{Al}_2\text{O}_3$ composite. The average crystallite size of the MoFe_2O_4 , Al_2O_3 , and $\text{MoFe}_2\text{O}_4/\text{Al}_2\text{O}_3$ samples was calculated using the Debye Scherrer formula given in Eq. (5) [33-35];

$$L = \frac{k\lambda}{\beta \cos\theta} \quad (5)$$

where, $k = 0.9$ (constant), $\lambda = 1.54 \text{ \AA}$, $\beta = \text{FWHM}$, $\theta = 2\theta/2$. L corresponds to the average size of crystallite (nm), β represents the full width at half maximum peak intensity (MoFe_2O_4 0.3989), (Al_2O_3 0.2001), ($\text{MoFe}_2\text{O}_4/\text{Al}_2\text{O}_3$ 0.1783) and θ is the Bragg's angle of diffraction.

The average crystallite sizes of MoFe_2O_4 particles, commercial Al_2O_3 and $\text{MoFe}_2\text{O}_4/\text{Al}_2\text{O}_3$ as a nanocomposite were found to be 23.97, 43.44, and 47.41 nm, respectively. The lattice parameter's value

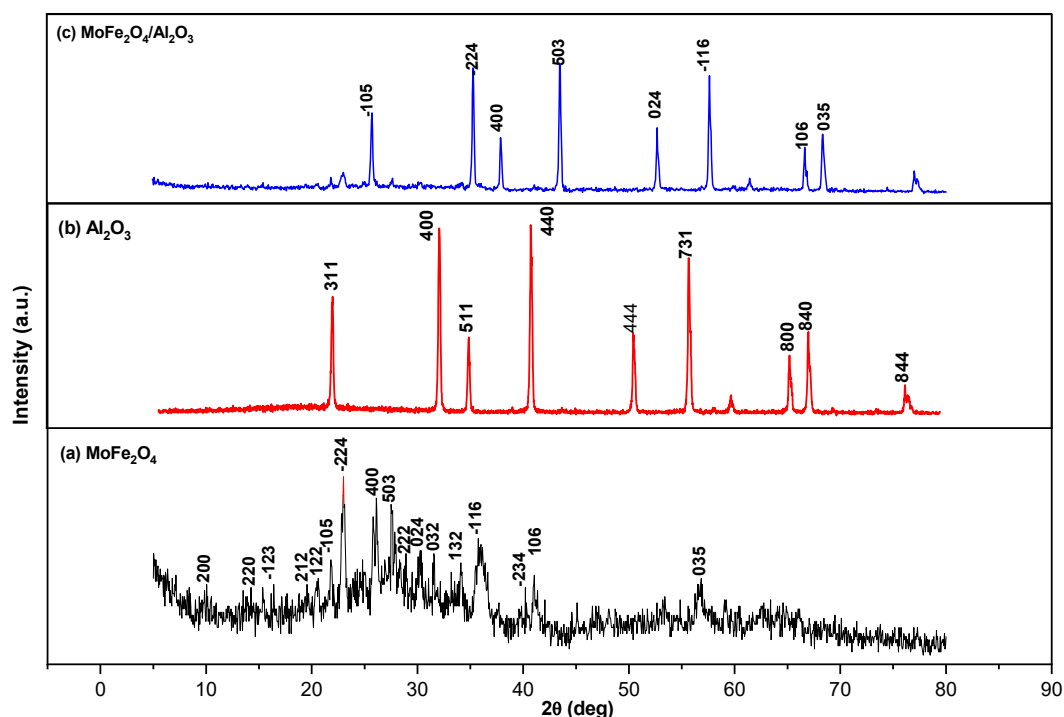


Fig 3. XRD pattern of (a) MoFe_2O_4 , (b) Al_2O_3 , (c) $\text{MoFe}_2\text{O}_4/\text{Al}_2\text{O}_3$ prepared in the presence of CT

depends on the difference in ionic radii of Fe^{3+} and Mo^{5+} ions. The tetrahedral ionic radius of Mo^{5+} ions (0.46 Å) is smaller than the tetrahedral ionic radius of Fe^{3+} ions (0.49 Å) and Al^{3+} (0.535 Å), while the octahedral ionic radius of Mo^{5+} ions (0.61 Å) is larger than the octahedral ionic radius of Fe^{3+} ions (0.55 Å) and Al^{3+} (0.535 Å) [36]. That mentality causes a metallic bond to form between two metals.

HR-SEM Analysis

The surface morphology of the as-prepared MoFe_2O_4 , nanocomposite surfaces ($\text{MoFe}_2\text{O}_4/\text{Al}_2\text{O}_3$) samples and commercial Al_2O_3 were examined by high-resolution scanning electron microscope (HR-SEM) analysis (FESEM FEI Nova Nano SEM 450). Fig. 4(a)

finds that the shape of synthesis MoFe_2O_4 is nano-plates, this result is in agreement with the result of XRD and works of literature [37]. Further, the spinel $\text{MoFe}_2\text{O}_4/\text{Al}_2\text{O}_3$ composites and Al_2O_3 resemble as like-popcorn shapes and like- brain cells. The prepared MoFe_2O_4 's particle size was increased from 36.86–46.99 to 42.03–49.88 nm in the nanocomposite, which is attributed to the Al_2O_3 being big particle size, which ranges from 76.49–89.15 nm, and Al is more ionic radius than the ionic radius of Mo and Fe.

EDX Analysis

The elemental compositions in (Fig. 5) of the as-synthesized MoFe_2O_4 , Al_2O_3 , and nanocomposite were confirmed by EDX analysis. The results demonstrated the

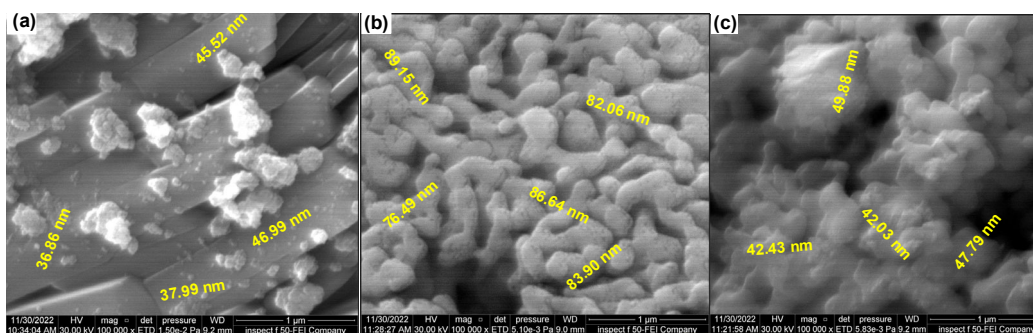


Fig 4. SEM images of (a) MoFe_2O_4 NPs, (b) Al_2O_3 , and (c) $\text{MoFe}_2\text{O}_4/\text{Al}_2\text{O}_3$ nanocomposites

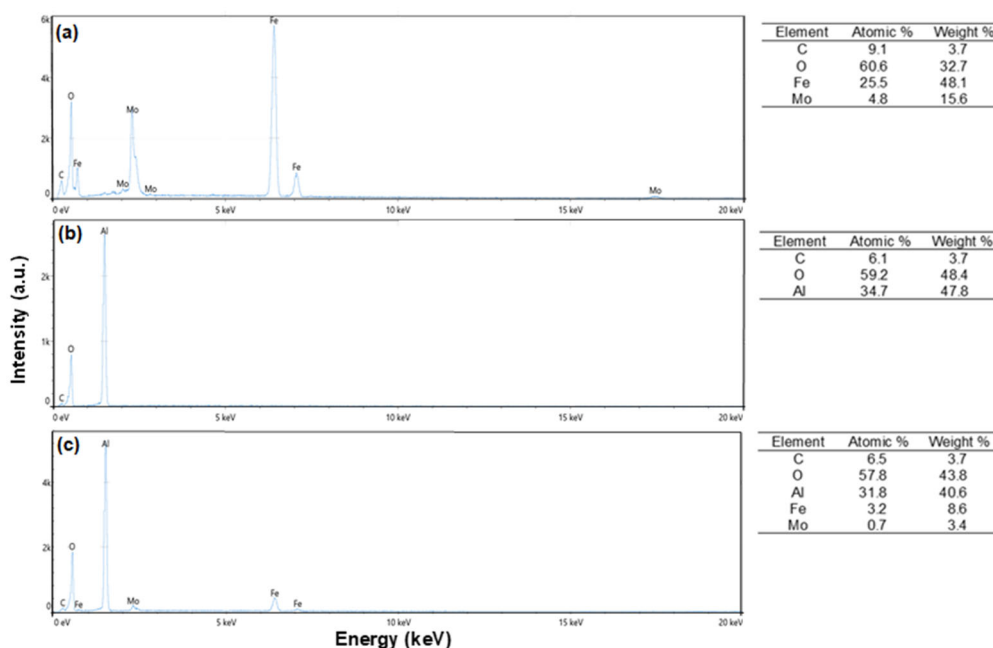


Fig 5. EDX spectra of (a) MoFe_2O_4 NPs, (b) Al_2O_3 and (c) $\text{MoFe}_2\text{O}_4/\text{Al}_2\text{O}_3$ nanocomposites

presence of all the compounds i.e., Fe, Mo, Al and O. That confirmed the formation of MoFe_2O_4 and its nanocomposite $\text{MoFe}_2\text{O}_4/\text{Al}_2\text{O}_3$ without any impurities.

The Mo, Fe, Al, and O signals are distinct and show those metal oxides containing iron, molybdenum, and aluminum are being processed actively. This is in good accord with the stoichiometry preparation ratio (2:1) that is utilized in the preparation technique. The peak strength of Al has increased for the samples prepared using larger Al precursor ratios.

FTIR Spectral Analysis

In order to analyze the surface structure and gain an understanding of chemical bonds, FTIR analysis was performed. The measured spectral span ranged from $4000\text{--}250\text{ cm}^{-1}$. The FTIR spectra of MoFe_2O_4 are displayed in Fig. 6. The hydroxyl group of the nanoparticles is responsible for extending the O–H band, which results in the characteristic band at 3291 cm^{-1} . The vibration band located at 2226.38 cm^{-1} is evidence for the C–H stretching of carbon, which was formed by the carbon residues at the material surfaces that had arisen from the combustion process. The strong and broadband

peaks that were positioned around $850\text{--}842\text{ cm}^{-1}$ can be assigned to the tetrahedral species of Mo in MoFe_2O_4 . The existence of the Mo–O–Mo bond was observed from the vibration band, which pointed in the region of $816\text{--}860\text{ cm}^{-1}$ [38]. The vibration band located about 824.14 cm^{-1} confirmed the coupling connection between oxygen and molybdenum. A weak band produced at $456\text{--}486\text{ cm}^{-1}$, which can be attributed to the Fe–O–Mo stretching vibration mode [39], can be attributed to the Mo–O asymmetrical stretching band that was found at about 541.53 cm^{-1} . The Al–O bond is also associated with a weak adsorption band at 722 cm^{-1} [40]. Table 1 shows how the vibration bands are assigned together with their wavenumber.

The Optical Property of Studied Photocatalyst

Based on Tauc Eq. (6) and the band gap (E_g) value for each photocatalyst sample, information regarding the material's potential as a photocatalyst was obtained. Here, h , v , k , t , A , and n are absorption coefficients, light, frequency, optical constant, thickness, absorbance, and constant values equal to 2 or $1/2$, respectively, for direct and indirect transitions are Plank's constants [41–42].

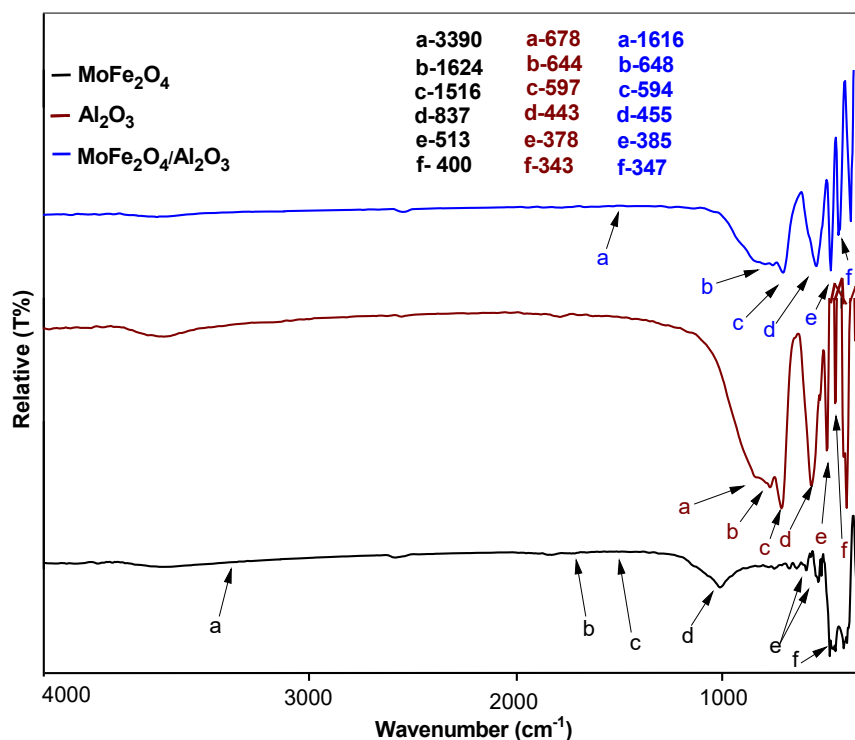


Fig 6. FTIR spectra of MoFe_2O_4 , Al_2O_3 , and $\text{MoFe}_2\text{O}_4/\text{Al}_2\text{O}_3$ nanocomposites

Table 1. Band assignments and related wavenumbers from FTIR spectra

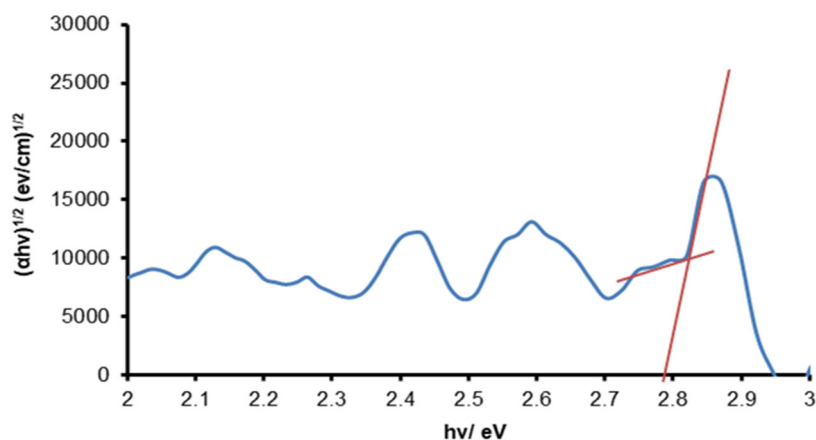
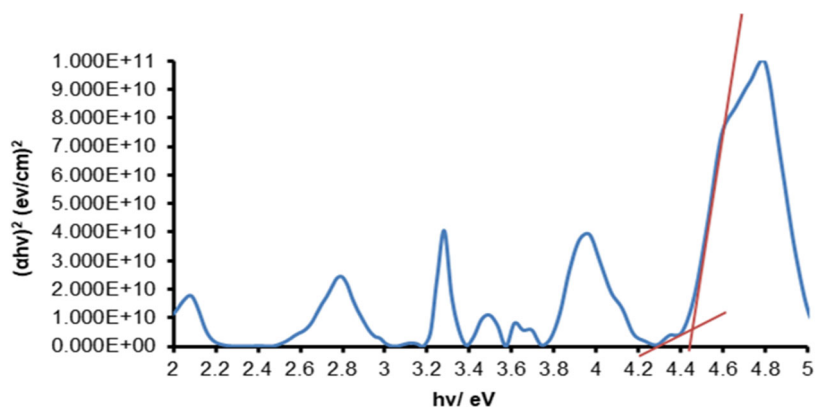
FTIR band wavenumber (cm ⁻¹)	Association bands type
456–486	Fe–O–Mo stretching vibration
594–648	O–Al–O stretching
541	Mo–O asymmetrical stretching in MoO ₄
824	Coupling bond between oxygen and molybdenum (O–Mo)
816–860	Mo–O–Mo bond
850–842	Tetrahedral species of Mo in MoFe ₂ O ₄
2226	C–H stretching
3293	O–H stretching

$$(\alpha h\nu)^{1/n} = k(h\nu - E_g) \quad (6)$$

$$\alpha = (2.3026A)/t \quad (7)$$

According to the plotted Tauc equation in Fig. 7, 8 and 9. that observed the band gap for MoFe₂O₄ is direct [29] and equal to 2.78 eV (445.986 nm), while it is an indirect band gap for the α -Al₂O₃ and MoF₂O₄/Al₂O₃ nanocomposite with magnitudes equal to 4.44 eV (279.243 nm) and 4.05 eV (306.133 nm), respectively. The

coupling α -Al₂O₃ during the production of a composite is useful due to raising the lightness of spinel MoFe₂O₄. This vital step to improve their optical properties when used as a photocatalyst because the spinel MoFe₂O₄ has a small band gap that may be increased the recombination process but the coupling process will decline that via increase the charge separation and increase the hydroxyl radical life [42-43].

**Fig 7.** Tauc plot for MoFe₂O₄ as a direct band gap**Fig 8.** Tauc plot for Al₂O₃ as an indirect band gap

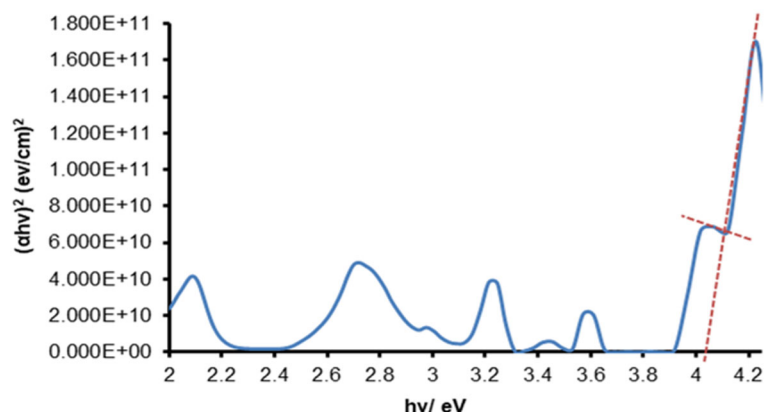


Fig 9. Tauc plot for $\text{MoFe}_2\text{O}_4/\text{Al}_2\text{O}_3$ as an indirect band gap

Photo Decolorization of Indigo Carmine (IC) Dye

The photo decolorization of organic dyes, IC, under UV light irradiation was performed to assess the photocatalytic activities of MoFe_2O_4 and its composite with alumina. IC dye was selected as a representative hazardous dye to assess the photocatalytic performance.

Fig. 10 and 11 explain the photocatalytic activity of MoFe_2O_4 , commercial Al_2O_3 , and $\text{MoFe}_2\text{O}_4/\text{Al}_2\text{O}_3$ composites. Fig. 11(a) explains the linear relation, and proves this reaction is pseudo-first order. The photo-decolorization percentage of IC dye increases after modifying the surface of MoFe_2O_4 with alumina from

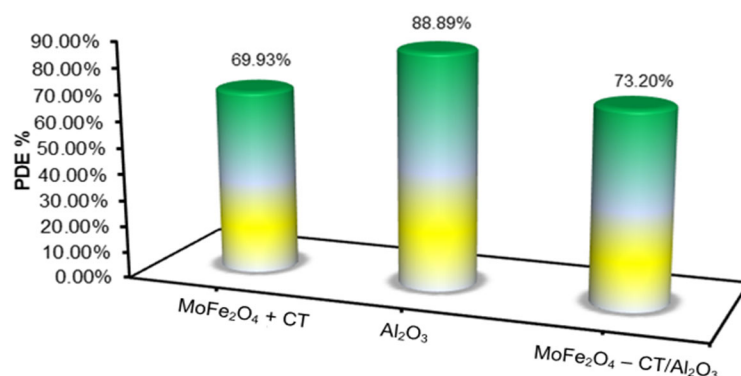


Fig 10. Relation of PDE% for photo decolorization of IC dye in all photocatalysts at 20 °C for 50 min

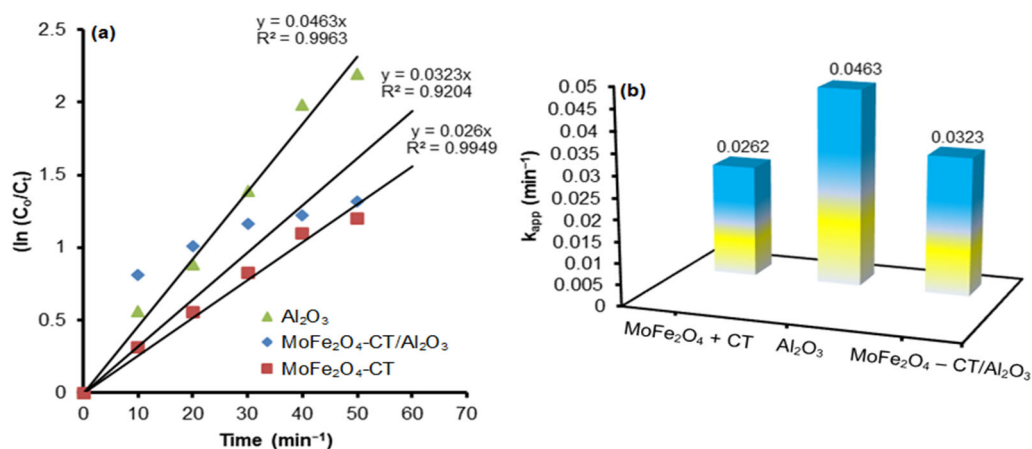


Fig 11. Kinetic of photo-decolorization of 25 ppm IC dye using 0.1 g of photocatalysts at 20 °C and pH 5.3 for 50 min. (a) Relation between $\ln(C_0/C_t)$ versus samples, and (b) relation of apparent rate constant versus time

69.934 to 73.202% after 50 min and 20 °C of UV-A light exposure. This is because the surface acidity is increased, allowing hydroxyl groups to adsorb and produce hydroxyl radicals via photoreaction. Alumina will also lighten the dark color of MoFe_2O_4 when added and increase the separation between positive and negative charges of exciton. After being altered under the same circumstances, the apparent rate constant for this photoreaction also increased. This cause is consistent with that which was mentioned in reference [43].

Effect of Process Variables on Decolorization

Effect of pH

Utilizing the pH effect, a crucial photocatalytic parameter that regulates the production of reactive species, it was calculated how much of this dye would be photo decolorized. MoFe_2O_4 , Al_2O_3 , and $\text{MoFe}_2\text{O}_4/\text{Al}_2\text{O}_3$ nanocomposite were used to adjust the IC dye's original pH. The initial pH of the solution will typically have an impact on the ionization state, the acid-base property of the photocatalyst surface, and the reactant dye [24]. Therefore, this effect was performed in Fig. 12. The lower value of the initial pH dye solution (pH = 5.3) gives the maximum decolorization of IC, because the dye has an acidic nature. And the PDE of IC were obtained at 10 °C for 50 min and equal to 90.84, 92.81, and 91.5% using MoFe_2O_4 , Al_2O_3 , $\text{MoFe}_2\text{O}_4/\text{Al}_2\text{O}_3$, respectively. It can be explained by the solid acid characteristics of MoFe_2O_4 , which are proved by both the low zero point charge (ZPC) and the presence of strong acid sites. The ZPC of MoFe_2O_4

is 2.94; beyond this, deprotonation occurs and an acidic microenvironment is formed on the surface of MoFe_2O_4 particles [30]. Also, the using of CT as a positive surfactant gives the best PDE results which is due to the acidity of the dye, so the attractive forces will increase on MoFe_2O_4 NP, which was prepared in the presence of a CT [44]. Moreover, by increasing the pH of a solution, more protons are subtracted from the surface of the $\text{MoFe}_2\text{O}_4 + \text{CT}$ NPs, leading to a more acidic medium. It compensates for the negative influence due to an increase in solution pH. In this case, the surface of $\text{MoFe}_2\text{O}_4 + \text{CT}$ NPs plays an acid–base buffering role. However, the current study found that when the solution pH is elevated to 9, the photocatalysis activity appears to decline. The description of a strongly alkaline situation that results from $\bullet\text{OH}$'s reduced capacity to oxidize could provide evidence for this occurrence [45].

Effect of temperature

The effect of reaction temperature on photocatalysts MoFe_2O_4 , Al_2O_3 , and $\text{MoFe}_2\text{O}_4/\text{Al}_2\text{O}_3$ nanocomposite were investigated. The photocatalytic processes sometimes do not depend on temperature, but in this case, it was found that the photocatalytic processes are affected by a change in temperature [46]. Therefore, to explore more about temperature-dependent decolorization of dyes, record decolorization time for IC dye at 10, 15, 20, and 25 °C using a 375 nm wavelength light source. The results in Fig. 13 were observed that the PED values decrease with increasing

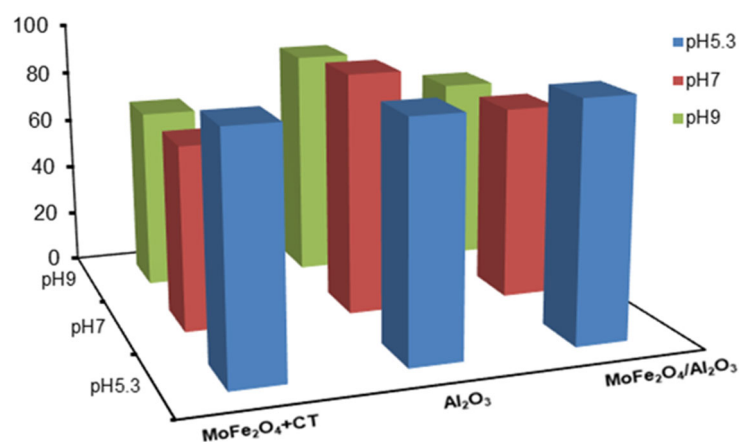


Fig 12. Relationship of PDE% vs. initial pH of studied IC dye. The experimental conditions include initial IC concentration of 25 ppm, photocatalyst dosage of 0.1 g at laboratory temperature (10 °C)

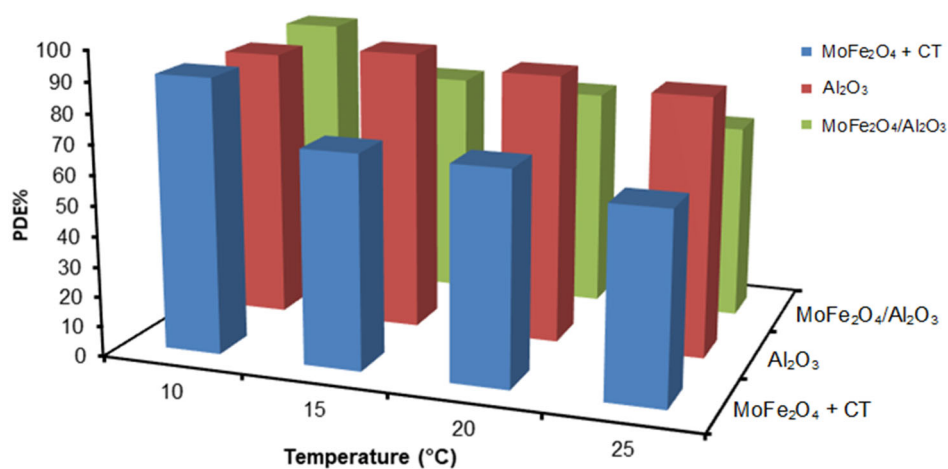


Fig 13. The relationship between PDE% vs temperatures of studied IC dye at pH 5.3

the temperature from 10 to 25 °C in the period of time from 10 to 50 min because this photoreaction is exothermic and this corresponds with another literature [43].

In accordance with this behavior, oxygen molecules (O₂) will be chemisorbed on the surface of MoFe₂O₄ and will capture free electrons from the MoFe₂O₄ conduction band to ionize into oxygen ions such as O₂⁻, O²⁻, and O⁻ depending on the temperature, in contrast to Al₂O₃, the

decrease in electron concentration on the surface of MoFe₂O₄ results in the formation of an electron depletion layer on the surface [47].

Through the effect of temperature on photocatalyst, the reaction is found to obey Arrhenius equation plot Eq. (8) in Fig. 14 and the Ering-Pollani equation plot Eq. (9) in Fig. 15 to find the activation energy (E_a), enthalpy (ΔH[#]) and entropy (ΔS[#]), respectively [48-49];

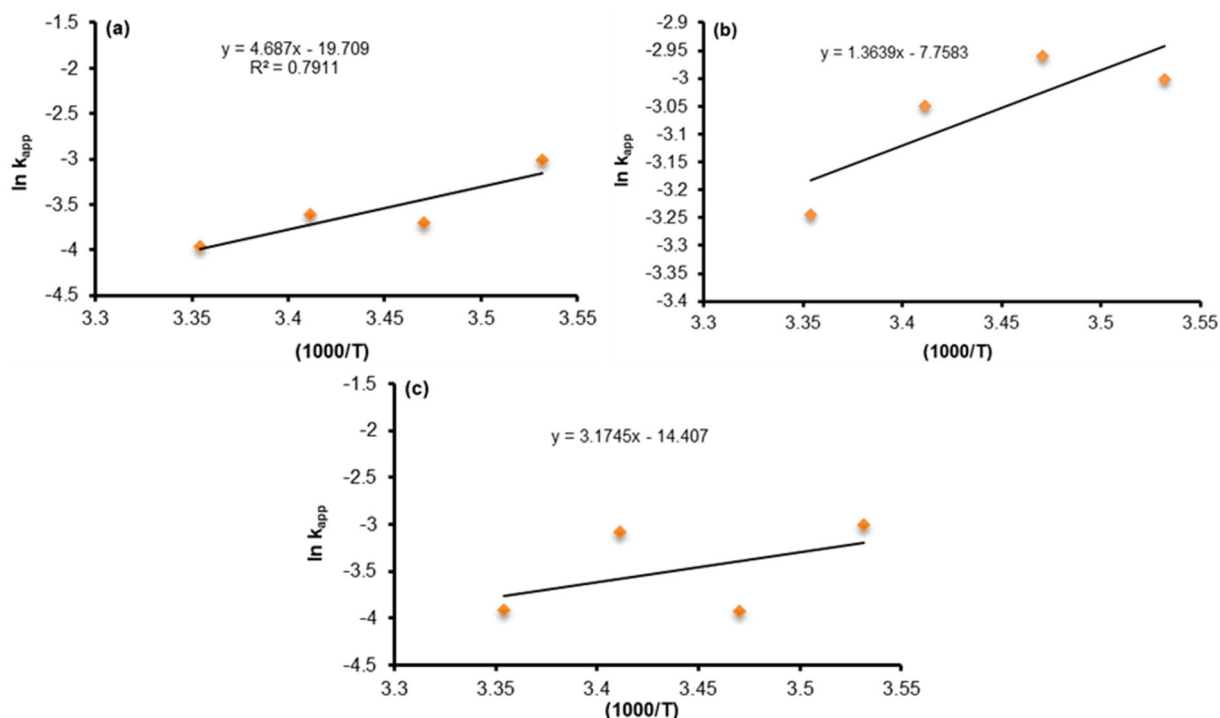


Fig 14. Arrhenius equation plot for photoreaction (a) MoFe₂O₄ + CT NPs, (b) Al₂O₃, and (c) MoFe₂O₄/Al₂O₃ nanocomposites

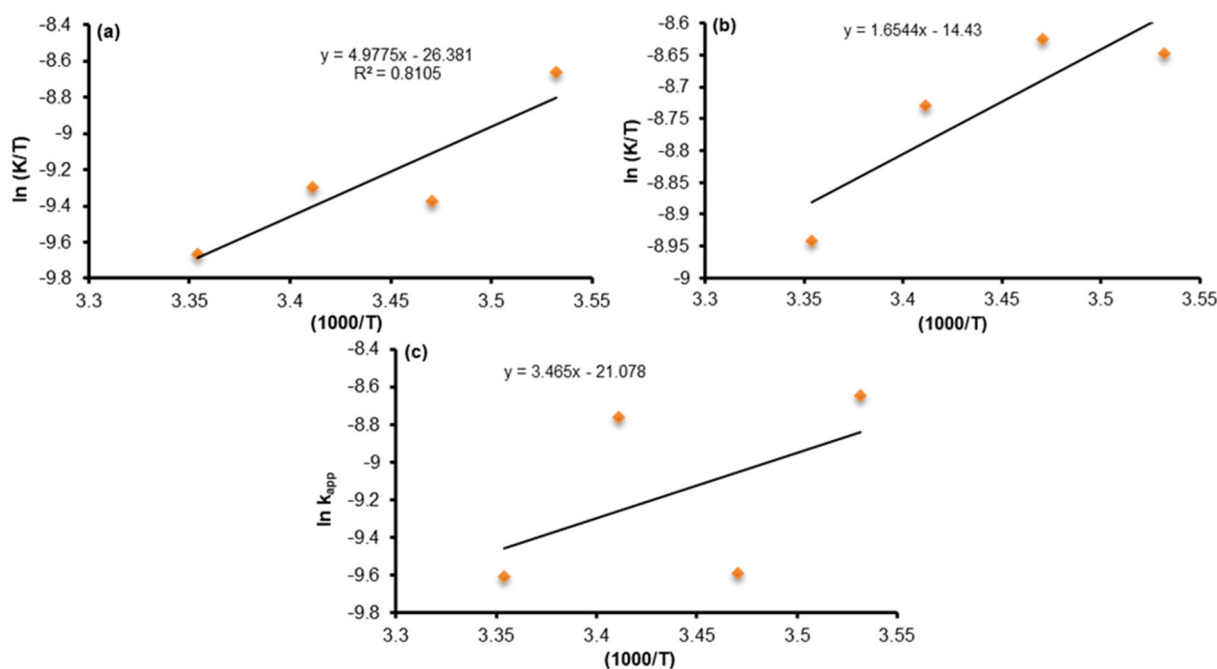


Fig 15. Eyring-Polanyi equation plot for photoreaction (a) MoFe_2O_4 + CT NPs, (b) Al_2O_3 , and (c) $\text{MoFe}_2\text{O}_4/\text{Al}_2\text{O}_3$ nanocomposites

Table 2. Activation parameters for the decolonization reaction of Indigo carmine with photocatalysts samples

Parameters	$E_a^\#$ (kJ mol ⁻¹)	$\Delta H^\#$ (kJ mol ⁻¹)	$\Delta S^\#$ (kJ mol ⁻¹)	$\Delta G^\#$ (kJ mol ⁻¹)
MoFe_2O_4 + CT NPs	-38.9677	-41.3830	-6.0309	-39.6280
Al_2O_3	-11.3395	-13.7550	-4.5935	-12.0000
$\text{MoFe}_2\text{O}_4/\text{Al}_2\text{O}_3$ NCs	-26.3928	-26.1250	-5.3931	-24.3700

$$\ln k_{\text{app}} = \frac{-E_a}{RT} + \ln A \quad (8)$$

$$\ln \left(\frac{k_{\text{app}}}{T} \right) = \frac{-\Delta H^\#}{RT} + \left(\ln \left(\frac{k_B}{h} \right) + \frac{\Delta S^\#}{R} \right) \quad (9)$$

where k_B is Boltzmann constant ($1.380649 \times 10^{-23} \text{ m}^2 \text{ kg s}^{-2} \text{ K}^{-1}$), and h is Planck constant ($6.626 \times 10^{-34} \text{ J s}$), A is frequency factor, R is gas constant ($8.314 \text{ J mol}^{-1} \text{ K}^{-1}$). The Gibbs energy Eq. (10) was calculated depending on the values of $\Delta S^\#$ and $\Delta H^\#$ [18].

$$\Delta G^\# = \Delta H^\# - T\Delta S^\# \quad (10)$$

The values of activation parameters $E_a^\#$, $\Delta S^\#$, $\Delta H^\#$, $\Delta G^\#$ are given in Table 2.

According to E_a value, Al_2O_3 has a large and negative E_a because of its large bandgap (the activation energy is more than the energy needed to transport an electron from the valance band to the conductive band). Spinel MoFe_2O_4 surface activation energies before and after

incorporation of Al_2O_3 were found to be negative values also. It might mean that the photoreaction will take place in several steps, one of which may be exothermic, before converting at a very low positive activation energy through a number of chain reactions [50]. Consequently, a fast binding step may occur on the Fe^{3+} position in the crystal lattice, but a less fast step (at a very low positive activation energy value) may be obtained on the Mo^{6+} position in the crystal lattice. This behavior investigates the spinel structure, which involves Fe^{3+} in tetrahedral and Mo^{6+} in octahedral hybridizes. By employing spinel and its structure, this situation causes negative enthalpy values to be produced. This situation is comparable to those described in the references [50]. According to the negative value of entropy, the transition state produced by the breakdown of this dye has less structural freedom than the reactant (dye molecule). According to discovered thermodynamic

theories, photoreaction is exothermic and spontaneous. The ΔS^\ddagger is also negative due to a depressing in randomness at the solid-solution interface via the IC decolonization and indicates that some structural exchange occurs among the active sites of the dye and ions [6,28].

■ CONCLUSION

The MoFe_2O_4 nanoplate was successfully prepared using a hydrothermal process. The morphology and structure were controlled by adding positive surfactants such as cetrimide (CT). The CT vesicles can serve as the soft template for the synthesis of structured MoFe_2O_4 nanoplate. The incorporation of MoFe_2O_4 with Al_2O_3 as a nanocomposite was done using the ultrasonic waves method. By using XRD analysis, FTIR and SEM-EDX, the nanoparticles are confirmed with spinel of MoFe_2O_4 . The composite shape occurred as like- popcorn nanoparticles. The catalytic performance of MoFe_2O_4 increases when Al_2O_3 is combined as the photoactivity in using the MoFe_2O_4 and composite with Indigo carmine dye at acidic pH equal to 5.3 with low temperature (10 °C). At the examined temperature range, the lower activation energy indicates to rise in the photodecolorization of IC dye as the negative values of ΔG^\ddagger and ΔH^\ddagger indicated the spontaneous and exothermic nature of the decolonization process. Moreover, the ΔS^\ddagger is also negative also.

■ ACKNOWLEDGMENTS

The authors would like to thank everyone who helped with this paper from the scientific faculty at the Department of Chemistry, University of Kerbala.

■ AUTHOR CONTRIBUTIONS

Mohammed Ali Hameed conducted the experiment, Mohammed Ali Hameed and Luma Majeed Ahmed conducted k_{app} , E% and, mean crystal size calculations, Luma Majeed Ahmed conducted band gaps calculations, Mohammed Ali Hameed and Luma Majeed Ahmed wrote and revised the manuscript. All authors agreed to the final version of this manuscript.

■ REFERENCES

- [1] Mohammad, H.M., Saeed, S.I., and Ahmed, L.M., 2022, Broccoli-like iron oxide nanoparticles

synthesis in presence of surfactants and using them in the removal of water-colored contamination, *J. Nanostruct.*, 12 (4), 1034–1048.

- [2] Abed, A.Q., Al Hindawi, A.M., and Alesary, H.F., 2023, Synthesis and characterization of zinc sulfide nanomaterials for removal methylene blue dye from aqueous solution, *AIP Conf. Proc.*, 2830, 020001.
- [3] Al-Abadi, S.I., Al-Da'amy, M.A., and Kareem, E.T., 2021, Thermodynamic study for removing of crystal violet dye on Iraqi porcelanite rocks powder, *IOP Conf. Ser.: Earth Environ. Sci.*, 790, 012055.
- [4] Gallo, R.D., Cariello, G., Goulart, T.A.C., and Jurberg, I.D., 2023, Visible light-mediated photolysis of organic molecules: The case study of diazo compounds, *Chem. Commun.*, 59 (48), 7346–7360.
- [5] Giwa, A.R.A., Bello, I.A., Olabintan, A.B., Bello, O.S., and Saleh, T.A., 2020, Kinetic and thermodynamic studies of Fenton oxidative decolorization of methylene blue, *Heliyon*, 6 (8), e04454.
- [6] Anisuzzaman, S.M., Joseph, C.G., Pang, C.K., Affandi, N.A., Maruja, S.N., and Vijayan, V., 2022, Current trends in the utilization of photolysis and photocatalysis treatment processes for the remediation of dye wastewater: A short review, *ChemEngineering*, 6 (4), 58.
- [7] Ahmad, R., Ahmad, Z., Khan, A.U., Mastoi, N.R., Aslam, M., and Kim, J., 2016, Photocatalytic systems as an advanced environmental remediation: Recent developments, limitations and new avenues for applications, *J. Environ. Chem. Eng.*, 4 (4, Part A), 4143–4164.
- [8] Abass, S.K., Al-Hilfi, J.A., Abbas, S.K., and Ahmed, L.M., 2020, Preparation, characterization and study of the photodecolorization of mixed-ligand binuclear Co(II) complex of Schiff base by ZnO, *Indones. J. Chem.*, 20 (2), 404–412.
- [9] Ghanbari, F., and Moradi, M., 2017, Application of peroxymonosulfate and its activation methods for degradation of environmental organic pollutants, *Chem. Eng. J.*, 310, 41–62.
- [10] Zheng, L., Han, S., Liu, H., Yu, P., and Fang, X., 2016, Hierarchical MoS_2 nanosheet@ TiO_2 nanotube array composites with enhanced

- photocatalytic and photocurrent performances, *Small*, 12 (11), 1527–1536.
- [11] Li, M., Wang, D., Li, J., Pan, Z., Ma, H., Jiang, Y., Tian, Z., and Lu, A., 2017, Surfactant-assisted hydrothermally synthesized MoS₂ samples with controllable morphologies and structures for anthracene hydrogenation, *Chin. J. Catal.*, 38 (3), 597–606.
- [12] Jiang, L., Yuan, X., Zeng, G., Wu, Z., Liang, J., Chen, X., Leng, L., Wang, H., and Wang, H., 2018, Metal-free efficient photocatalyst for stable visible-light photocatalytic degradation of refractory pollutant, *Appl. Catal., B*, 221, 715–725.
- [13] Li, X., Xia, J., Zhu, W., Di, J., Wang, B., Yin, S., Chen, Z., and Li, H., 2016, Facile synthesis of few-layered MoS₂ modified BiOI with enhanced visible-light photocatalytic activity, *Colloids Surf., A*, 511, 1–7.
- [14] Zhang, S., Gu, P., Ma, R., Luo, C., Wen, T., Zhao, G., Cheng, W., and Wang, X., 2019, Recent developments in fabrication and structure regulation of visible-light-driven g-C₃N₄-based photocatalysts towards water purification: A critical review, *Catal. Today*, 335, 65–77.
- [15] Choudhury, S., Baeg, J.O., Park, N.J., and Yadav, R.K., 2012, A photocatalyst/enzyme couple that uses solar energy in the asymmetric reduction of acetophenones, *Angew. Chem., Int. Ed.*, 51 (46), 11624–11628.
- [16] Roopan, S.M., Elango, G., Priya, D.D., Asharani, I.V., Kishore, B., Vinayprabhakar, S., Pragatheshwaran, N., Mohanraj, K., Harshpriya, R., Shanavas, S., and Acevedo, R., 2019, Sunlight mediated photocatalytic degradation of organic pollutants by statistical optimization of green synthesized NiO NPs as catalyst, *J. Mol. Liq.*, 293, 111509.
- [17] Zhao, Y., Zhang, X., Wang, C., Zhao, Y., Zhou, H., Li, J., and Jin, H., 2017, The synthesis of hierarchical nanostructured MoS₂/graphene composites with enhanced visible-light photo-degradation property, *Appl. Surf. Sci.*, 412, 207–213.
- [18] Abd Zaid, A.A., Ahmed, L.M., and Mohammad, R.K., 2022, Synthesis of inverse spinel nickel ferrite like-broccoli nanoparticle and thermodynamic study of photo-decolorization of alkali blue 4B dye, *J. Nanostruct.*, 12 (3), 697–710.
- [19] Abd Zaid, A.A., Ahmed, L.M., and Mohammad, R.K., 2023, Solvothermal-assisted cushy precipitation method of like-cauliflower zinc ferrite (ZnFe₂O₄) nanoparticles using hexamethylenetetramine (hexamine) as a non-ionic surfactant, *J. Nanostruct.*, 13 (1), 193–203.
- [20] Roy, A., Kumar, S., Banerjee, D., and Ghose, J., 2000, Mössbauer studies on titanium substituted molybdenum ferrite, *Solid State Commun.*, 114 (3), 143–148.
- [21] Domenichini, B., Gillot, B., and Tailhades, P., 1992, Study by electrical conductivity, derivative thermogravimetry, infrared spectrometry and X-ray photoelectron spectroscopy of oxidation process of Fe₂MoO₄ in relation to the cationic distribution, *Thermochim. Acta*, 205, 259–269.
- [22] Mikhaylov, V.I., Krivoschapkina, E.F., Belyy, V.A., Isaenko, S.I., Zhukov, M.V., Gerasimov, E.Y., and Krivoschapkin, P.V., 2019, Magnetic mesoporous catalytic and adsorption active Fe-Al₂O₃ films, *Microporous Mesoporous Mater.*, 284, 225–234.
- [23] Zaouak, A., Noomen, A., and Jelassi, H., 2018, Gamma-radiation induced decolorization and degradation on aqueous solutions of Indigo Carmine dye, *J. Radioanal. Nucl. Chem.*, 317 (1), 37–44.
- [24] Hussain, Z.A., Fakhri, F.H., Alesary, H.F., and Ahmed, L.M., 2020, ZnO based material as photocatalyst for treating the textile anthraquinone derivative dye (dispersive blue 26 dye): Removal and photocatalytic treatment, *J. Phys.: Conf. Ser.*, 1664 (1), 012064.
- [25] Ridha, N.J., Mohamad Alosfur, F.K., Kadhim, H.B.A., and Ahmed, L.M., 2021, Synthesis of Ag decorated TiO₂ nanoneedles for photocatalytic degradation of methylene blue dye, *Mater. Res. Express*, 8 (12), 125013.
- [26] Karam, F.F., Hussein, F.H., Baqir, S.J., Halbus, A.F., Dillert, R., and Bahnemann, D., 2014, Photocatalytic degradation of anthracene in closed system reactor, *Int. J. Photoenergy*, 2014, 503825.

- [27] Jalaw Khan, R.S., Alosfur, F.K.M., and Abdul-Lettif, A.M., 2022, Characterization of pure anatase TiO₂ nano rods synthesized by microwave method, *AIP Conf. Proc.*, 2547 (1), 030020.
- [28] Obaid, A.J., and Ahmed, L.M., 2022, TiO₂ - catalyzed photo decolorization of chlorazol black BH dye under UV-A light, *AIP Conf. Proc.*, 2547 (1), 040011.
- [29] Tamilarasi, S., Balakrishnan, K., Muthuvel, I., Rajachandrasekar, T., Gowthami, K., and Thirunarayanan, G., 2020, Highly solar active Fe₂(MoO₄)₃ nanocatalyst assisted degradation of rhodamine-B dye, *J. Adv. Sci. Res.*, 11 (02), 93–100.
- [30] Parveen, S., Bhatti, I.A., Ashar, A., Javed, T., Mohsin, M., Hussain, M.T., Khan, M.I., Naz, S., and Iqbal, M., 2020, Synthesis, characterization and photocatalytic performance of iron molybdate (Fe₂(MoO₄)₃) for the degradation of endosulfan pesticide, *Mater. Res. Express*, 7 (3), 35016.
- [31] Casillas, J.E., Campa-Molina, J., Tzompantzi, F., Carbajal Arízaga, G.G., López-Gaona, A., Ulloa-Godínez, S., Cano, M.E., and Barrera, A., 2020, Photocatalytic degradation of diclofenac using Al₂O₃-Nd₂O₃ binary oxides prepared by the sol-gel method, *Materials*, 13 (6), 1345.
- [32] Zou, S., Luo, J., Lin, Z., Fu, P., and Chen, Z., 2018, Acetone gas sensor based on iron molybdate nanoparticles prepared by hydrothermal method with PVP as surfactant, *Mater. Res. Express*, 5 (12), 125013.
- [33] Kharaji, A.G., Shariati, A., and Takassi, M.A., 2013, A novel γ -alumina supported Fe-Mo bimetallic catalyst for reverse water gas shift reaction, *Chin. J. Chem. Eng.*, 21 (9), 1007–1014.
- [34] Mustapha, S., Ndamitso, M.M., Abdulkareem, A.S., Tijani, J.O., Shuaib, D.T., Mohammed, A.K., and Sumaila, A., 2019, Comparative study of crystallite size using Williamson-Hall and Debye-Scherrer plots for ZnO nanoparticles, *Adv. Nat. Sci.: Nanosci. Nanotechnol.*, 10 (4), 045013.
- [35] Abed, Z., Mohammad, R.K., and Elttayef, A., 2022, Structural properties of Ag-CuO thin films on silicon prepared via DC magnetron sputtering, *Egypt. J. Chem.*, 65 (4), 685–691.
- [36] Ghosh, D.C., and Biswas, R., 2003, Theoretical calculation of absolute radii of atoms and ions. Part 2. The ionic radii, *Int. J. Mol. Sci.*, 4 (6), 379–407.
- [37] Ramachandran, K., Chidambaram, S., Baskaran, B., Muthukumarasamy, A., and Lawrence, J.B., 2017, Investigations on structural, optical and magnetic properties of solution-combustion-synthesized nanocrystalline iron molybdate, *Bull. Mater. Sci.*, 40 (1), 87–92.
- [38] Ghorbani-Choghmarani, A., Mohammadi, M., Shiri, L., and Taherinia, Z., 2019, Synthesis and characterization of spinel FeAl₂O₄ (hercynite) magnetic nanoparticles and their application in multicomponent reactions, *Res. Chem. Intermed.*, 45 (11), 5705–5723.
- [39] Al-Mokdad, F., Hassan, R.S., and Awad, R., 2019, Physical and dielectric properties of MnFe₂O₄ doped by Mo, *Curr. Nanomater.*, 4 (2), 125–136.
- [40] Seevakan, K., Manikandan, A., Devendran, P., Antony, S.A., and Alagesan, T., 2016, One-pot synthesis and characterization studies of iron molybdenum mixed metal oxide (Fe₂(MoO₄)₃) nano-photocatalysts, *Adv. Sci. Eng. Med.*, 8 (7), 566–572.
- [41] Mursyalaat, V., Variiani, V.I., Arsyad, W.O.S., and Firihi, M.Z., 2023, The development of program for calculating the band gap energy of semiconductor material based on UV-vis spectrum using Delphi 7.0, *J. Phys.: Conf. Ser.*, 2498 (1), 012042.
- [42] Fakhri, F.H., and Ahmed, L.M., 2019, Incorporation CdS with ZnS as composite and using in photo-decolorization of Congo red dye, *Indones. J. Chem.*, 19 (4), 936–943.
- [43] Kadhim, H., Ahmed, L., and AL-Hachamii, M., 2022, Facile synthesis of spinel CoCr₂O₄ and its nanocomposite with ZrO₂: Employing in photocatalytic decolorization of Fe(II)-(luminol-tyrosine) complex, *Egypt. J. Chem.*, 65 (1), 481–488.
- [44] Iqbal, M., and Bhatti, I.A., 2015, Gamma radiation/H₂O₂ treatment of a nonylphenol ethoxylates: Degradation, cytotoxicity, and mutagenicity evaluation, *J. Hazard. Mater.*, 299, 351–360.

- [45] Singh, B., Singh, P., Siddiqui, S., Singh, D., and Gupta, M., 2022, Wastewater treatment using Fe-doped perovskite manganites by photocatalytic degradation of methyl orange, crystal violet and indigo carmine dyes in tungsten bulb/sunlight, *J. Rare Earths*, 41 (9), 1311–1322.
- [46] Aamir, M., Bibi, I., Ata, S., Majid, F., Kamal, S., Alwadai, N., Sultan, M., Iqbal, S., Aadil, M., and Iqbal, M., 2021, Graphene oxide nanocomposite with Co and Fe doped LaCrO_3 perovskite active under solar light irradiation for the enhanced degradation of crystal violet dye, *J. Mol. Liq.*, 322, 114895.
- [47] Tandel, A.V., and Padhiyar, N.B., 2015, Kinetics of oxidation of indigo carmine by vanadium (V) in presence of surfactants, *Res. J. Chem. Sci.*, 5 (11), 24–30.
- [48] Rezaei, M., and Nezamzadeh-Ejhieha, A., 2020, The ZnO-NiO nano-composite: a brief characterization, kinetic and thermodynamic study and study the Arrhenius model on the sulfasalazine photodegradation, *Int. J. Hydrogen Energy*, 45 (46), 24749–24764.
- [49] Sidney Santana, C., Nicodemos Ramos, M.D., Vieira Velloso, C.C., and Aguiar, A., 2019, Kinetic evaluation of dye decolorization by Fenton processes in the presence of 3-hydroxyanthranilic acid, *Int. J. Environ. Res. Public Health*, 16 (9), 1602.
- [50] Sekar, A., and Yadav, R., 2021, Green fabrication of zinc oxide supported carbon dots for visible light-responsive photocatalytic decolourization of Malachite Green dye: Optimization and kinetic studies, *Optik*, 242, 167311.